ACS APPLIED MATERIALS & INTERFACES

www.acsami.org

Research Article

# The Role of the Metal-Ion Charge in Mineral Interface Doping

Roman Konoplev-Esgenburg, Meike Koenig, Alexander Welle, Andreas Bogner, Roberto C. Longo, and Peter Thissen*

**Cite This:** https://doi.org/10.1021/acsami.5c09080 **Read Online**

ACCESS | Metrics & More | Article Recommendations | Supporting Information

**ABSTRACT:** In this paper, we investigate the mineral interface doping (MID) process of silicon substrates, using various minerals to explore the role of the metal ions involved. Specifically, we use metal ions with +1, +2, and +3 charge states to determine whether the observed effects are unique to individual metals or if they reflect broader trends within charge groups. Silicon wafers are coated with different minerals and doped by rapid thermal annealing (RTA). The process is subsequently analyzed as a function of temperature using time-of-flight secondary-ion mass spectrometry (ToF-SIMS), infrared spectroscopy (IR), and electrochemical impedance spectroscopy (EIS). To unravel the underlying atomistic mechanisms, we perform density functional theory (DFT) simulations, obtaining the kinetic activation energies of the corresponding doping processes and their dependence on metal valence. Our findings reveal that the required doping temperature decreases with the charge density of metal ions; however, there is a required minimum temperature to achieve the diffusion of phosphorus into the silicon bulk. During the MID process, metal silicates are first formed at the interface, while the atomic phosphorus constituents diffuse into the silicon substrate. Finally, the metal silicates are removed postdoping using nontoxic acids, thus making the process broadly applicable.

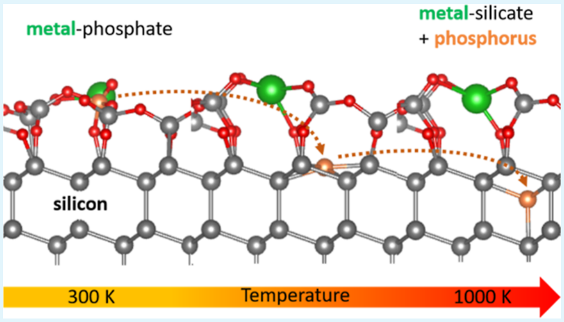

**KEYWORDS:** *silicon, doping, mineral, metal, charge, infrared, DFT*

## 1. INTRODUCTION

Electronic devices are irrevocably integrated into our lives.[1] As the semiconductor industry is going through a swift expansion, the resulting progress and innovation directly influence subsequent industries. Semiconductor research focuses mainly on developing efficient and cost-effective manufacturing materials that are not always environmentally friendly. Both a limited lifetime and an often-improvised disposal demand are detrimental to the realization of a green electronic future. Therefore, research must shift its focus on substituting nondegradable and difficult-to-recycle materials to allow either biodegradation or facile recycling of electronic devices. Within this context, monolayer doping (MLD) has emerged as a substantial improvement toward the electrical activation of silicon substrates.[2−6] MLD is a well-controlled, wafer-scale, and surface doping technique first developed at the University of California, Berkeley, in 2007.[4] Attaining controlled doping of nanoscale semiconductor materials with atomic accuracy cannot be easily obtained by other existing technologies. MLD is currently used for fabricating ultrashallow junctions (USJs),[5] to be used as the heavily doped source/drain (S/D) contacts of metal oxide-semiconductor field effect transistors (MOSFETs), as well as for enabling the dopant profiling of nanostructures. The semiconductor industry is still dominated by silicon, including photovoltaics and integrated circuits. Silicon wafers are easy to fabricate, also displaying excellent electrical and mechanical properties, and forming high-quality insulating thermal oxides. In this work, we aim to extend the research of doping processes of silicon wafers without making use of any highly toxic chemical substances, a process referred to as mineral interface doping (MID).[7]

MID is an incipient method based on the deposition of a mineral containing the dopant of interest in a silicon wafer, followed by a rapid thermal annealing (RTA) step.[7] MID can utilize a variety of minerals that effectively form metal silicates in contact with silicon oxide. For this specific application, a mineral should consist of three components: a metal ion ($K^+$, $Mg^{2+}$, $Ce^{3+}$, ...), element that can be a source of electrons or holes in silicon bulk (such as P, As, B, etc.) and oxygen/chlorine components. For example, Thissen and Longo[7] investigated MID using hydroxyapatite ($Ca_5(PO_4)_3(OH)$). Most of the metal ions, as well as oxygen and chlorine, have very limited solubility in silicon at high temperatures, which thermodynamically favors them remaining in the surface oxide

**Received:** May 7, 2025
**Revised:** July 31, 2025
**Accepted:** August 5, 2025

layer rather than diffusing into the silicon substrate.[8,9] In the specific case of MID using hydroxyapatite, the formation of wollastonite ($CaSiO_3$) at the surface suggests that the native silicon oxide available at the surface wafer reacts with the metal ion, consuming metal ions and the oxygen/chlorine component. Such a process is mainly thermodynamically driven and has already been investigated using the example of wollastonite, as one of the most stable calcium silicate phases.[8,9] The main advantage of the formation of such metal-silicate phases as reaction byproducts is that they do not have to be etched with highly toxic hydrofluoric acid.

Compared with conventional doping methods, such as monolayer doping (MLD) and ion implantation, the mineral interface doping (MID) strategy presented here offers a fundamentally different approach. While MLD enables atomic-level control and smooth dopant profiles via self-limiting reactions and ion implantation allows for deep controlled doping using precise beam energies, both techniques require sophisticated vacuum tools and high-purity precursors, often under harsh or toxic conditions.

MID, by contrast, operates under ambient conditions using mineral precursors that are often inexpensive, nontoxic, and structurally diverse. This opens up a wide combinatorial design space for tailored doping profiles and surface interactions. However, current limitations include the sensitivity of the process to mineral properties (e.g., solubility, particle size) and deposition behavior, which can result in a nonuniform surface coverage and variable doping efficiencies. These aspects are still under exploration and currently limit the direct scalability of the process. Nonetheless, the approach provides a promising sustainable alternative for surface doping and merits further development.

With respect to the list of raw materials that can be used in a MID process, the new International Mineralogical Association (IMA) List of Minerals includes selected information on the 5237 currently classified species,[10] including 813 phosphate minerals. According to the Nickel−Strunz Classification (10th Edition[11]), phosphate minerals are defined by containing the tetrahedrally coordinated phosphate ($PO4^{3-}$) anion, along with the freely substituting arsenate ($AsO_4^{3-}$) and vanadate ($VO_4^{3-}$). Chlorine ($Cl^-$), fluorine ($F^-$), and hydroxide ($OH^-$) anions can also fit into the crystal structure. Among phosphate minerals, apatite is one of the best-known representatives of the phosphate group, being more important to a wider group of disciplines of study than any other mineral.[12] On the basis of the chemical composition, the apatite supergroup is divided into five groups: apatite, hedyphane, belovite, britholite, and ellestadite groups.[13] The apatite supergroup includes minerals with a generic chemical formula of ${}^{IX}M1_2{}^{VII}M2_3({}^{IV}TO_4)_3X$ ($Z = 2$).[14] Overall, phosphate minerals can be grouped as (i) primary phosphates that have crystallized from the liquid phase; (ii) secondary phosphates formed by the alteration of primary phosphates; and (iii) fine-grained rock phosphates formed at low temperatures from phosphorus-bearing organic material, primarily underwater.

The deposition of the mineral on the semiconductor surface is performed via the tethering and aggregation by growth (T-BAG) method, which was specifically developed for the deposition of self-assembled monolayers (SAMs) of organophosphonic acids on native silicon oxide surfaces.[15] The T-BAG method was recently extended to lamellar structured minerals[16] and, as mentioned above, adapted for particles of hydroxyapatite.[7] The T-BAG process involves the preparation of a liquid dispersion of phosphate mineral particles, followed by the subsequent evaporation of the liquid, resulting in the deposition of a thin film of mineral particles on the silicon wafer. MID provides several advantages over MLD. As described above, multilayers of mineral particles can be deposited on the silicon surface, which leads to an increased concentration of the dopant that can diffuse into the silicon during annealing. MLD is, in practice, limited to the amount of the dopant that can be deposited within a single monolayer. MLD also faces the problem of carbon contamination, which is inevitably introduced into the silicon bulk by diffusion during annealing. On the contrary, the use of inorganic phosphates in MID will reduce the carbon contamination of the system.

As it was recently highlighted, the direct attachment of dopants on silicon wafer is possible via the tethering by aggregation and growth (T-BAG) processes, which was first developed for the deposition of SAMs of organophosphonic acids.[15] The main disadvantage of this process is the long time necessary to complete it, typically more than 48 h. Recent investigations show that the method is suitable and reproducible for lamellar-structured minerals such as montmorillonite.[16] Additionally, the T-BAG method is successfully utilized for the deposition of hydroxyapatite.[7] In situ characterization methods are developed to monitor the chemical evolution of the layer as a function of the temperature and to explore the role of the environment after the initial wet deposition on the oxide surface. However, the T-BAG method is not without inherent limitations. While the employed method is simple and efficient, also offering expediency in sample preparation as well as allowing the use of a diverse set of minerals, it is crucial to acknowledge its propensity for the nonuniform distribution of dopants over the semiconductor material; thus, the necessity for careful consideration and refinement in future doping strategies.[17−19] Surprisingly, there has been little progress in understanding the grafting mechanism, and little attention paid to the role of the environment.

In this work, we investigate the correlation between mineral components, more specifically, the metal cations, and the required temperature for inducing structural changes in the phosphates and subsequent diffusion of phosphorus into the silicon lattice. Selected systems include $Ca_5(PO_4)_3(OH)$, $KH_2PO_4$, $MgNH_4PO_4{\cdot}6H_2O$, and $CePO_4$. To study the atomistic details of metal silicate formation and the driving force for phosphorus diffusion through the oxide into the silicon lattice, density-functional theory (density functional theory (DFT)) simulations were used to determine minimum energy pathways and the kinetic activation barrier for the different metal cations studied. Finally, etching procedures were also investigated to demonstrate the viability of etching without the use of toxic HF. MID offers the possibility of utilizing a broad range of minerals that can be used as dopants and eliminate carbon contamination.

## 2. MATERIALS AND METHODS

**2.1. Sample Preparation.** A 3 cm × 1 cm (500 μm thick and double-side polished) p-type (boron-doped, resistivity of 24−34 Ω cm) Cz silicon (111) wafer was first chemically cleaned with a 30 min exposure at 80 °C to a 1:3 solution of aqueous $H_2O_2$ (30%)/18 M $H_2SO_4$ (hereafter referred to as a piranha solution) prepared with 98% sulfuric acid used as received from Merck KGaA to remove organic contamination. The wafer was rinsed with deionized water and dried with $N_2$. Subsequently, the silicon wafer was immersed in a dispersion of 7 mL of tetrahydrofuran (THF) and a phosphate

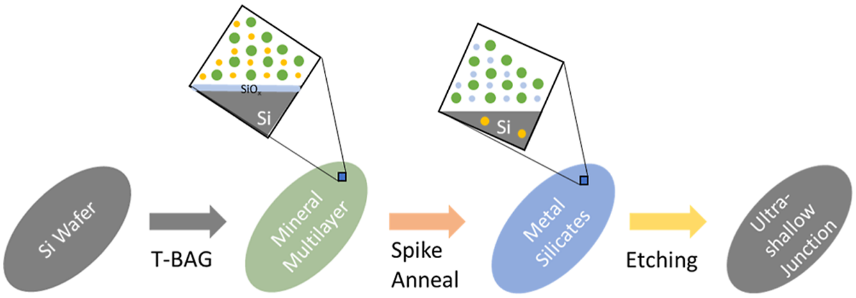

**Figure 1.** Schematic representation of (1) deposition of mineral multilayers via T-BAG with a layer at the interface, (2) diffusion of phosphorus into the Si lattice via MID and formation of silicates on the silicon surface, and (3) subsequent etching with an option of repeating the cycle or use in the further fabrication process of electronic devices.

mineral (hydroxyapatite (HAp, $Ca_5(PO_4)_3(OH)$), 0.0008 g with 99% of pureness from Omikron GmbH; cerium(III)phosphate ($CePO_4$), 0.0008 g with 99% pureness from thermo scientific; potassium phosphate monobasic ($KH_2PO_4$), 0.0011 g with 98.0% pureness from thermo scientific; ammonium magnesium phosphate hexahydrate ($MgNH_4PO_4·6H_2O$), 0.0010 g with 98% pureness from thermo scientific). The THF was evaporated at 60 °C until complete evaporation (≈2 h) of the liquid and the phosphate minerals covered both sides of the wafer surface.[15,16,20]

The coated wafer was mounted on a heatable sample holder made of tantalum under an ultrahigh vacuum and analyzed with IR transmission spectroscopy. The temperature of the samples was increased stepwise from room temperature to temperatures in the range between 700 and 800 °C, whereas the spectra were recorded at room temperature (RT). All temperature readings are monitored by a Eurotherm unit using type-K thermocouples spot-welded to a Ta clip attached to the sample edge. Previous calibrations[21] with a pyrometer indicate that the thermocouple readings are systematically too low (∼20−50 °C) in the 500−900 °C range. However, this is a systematic error; therefore, the relative measures are reproducible.

**2.2. Fourier Transform Infrared Spectroscopy (FT-IR).** The Fourier transform infrared spectroscopy (FT-IR) spectra were recorded on a Bruker Vertex V70 spectrometer equipped with a deuterated-triglycine sulfate (DTGS) detector. 1024 scans in the 7500−400 $cm^{-1}$ spectral range were recorded with a resolution of 4 $cm^{-1}$. Then, IR data are presented as differential spectra, calculated as $-\lg(T_1/T_2)$, where $T_1$ and $T_2$ are single-channel transmission spectra before and after the temperature-dependent process, respectively. This approach highlights spectral changes directly linked to the phosphorus doping process and avoids artifacts arising from baseline fluctuations, source instability, or environmental interference.

**2.3. Spectroscopic Ellipsometry (SE).** Spectroscopic ellipsometry measurements were performed with a M2000 instrument (Woollam Co., Inc., Lincoln NE, USA). All measurements were performed in the spectral region of 360−1000 nm at three angles of incidence (AOI = 55, 65, 75°). To evaluate the experimental data, a multilayer optical box model was applied using Complete EASE (Version 6.70) software provided by the manufacturer of the instrument. Silicon substrates were fitted with database values for Si and $SiO_2$. The thickness of the hydroxyapatite layer was fitted using a Cauchy-dispersion with fixed model parameters $A = 1.65$ and $B = 0.01$.

**2.4. Electrochemical Impedance Spectroscopy (EIS).** Impedance spectroscopy of the coated wafer before and after heating at 900 °C was performed using an IMPEDANCE ANALYZER IM3570 (HIOKI) R, L, C measuring device operated at room temperature in the frequency range of 8 Hz−8 MHz, using tantalum clamping contacts with a diameter of 1 mm.

**2.5. ToF-SIMS).** The time-of-flight secondary ion mass spectrometry (ToF-SIMS) analysis was carried out on a gridless reflectron-based ToF-SIMS V (ION-TOF GmbH, Muenster, Germany), equipped with a bismuth-cluster ion source. All spectra and images were obtained using $Bi^+$ primary ions at 25 keV energy in the high current bunched mode, with a mass resolution of $m/\Delta m \geq 6000$ @ $^{30}Si$. The beam diameter was ≈3−5 $\mu$m. The Bi primary beam was rastered on a 250 × 250 $\mu m^2$ field of view and 128 × 128 pixels were recorded. Depth profiling was performed in the full interlaced mode either with 0.5 keV energy $Cs^+$ beam (40 nA target current), rastered across 500 × 500 $\mu m^2$, or a 1 keV $Cs^+$ beam (114 nA) scanned over 350 × 350 $\mu m^2$. The measured data was transformed into quantitative values with the help of the NIST Standard Reference Material, 2133, phosphorus implant in the silicon depth profile standard via the determination of sputter yields of bulk silicon and sensitivity factors of $P^-$ in bulk Si.

**2.6. Micro-X-ray Fluorescence ($\mu$XRF).** The investigations were carried out with a Bruker M4 TORNADO $\mu$XRF instrument (Bruker Nano GmbH, Berlin, Germany) using a rhodium target to generate the high-energy radiation, a polycapillary lens with a spot size of 25 $\mu$m, and a 30 $mm^2$ silicon drift detector (SDD) for the energy-dispersive detection of the fluorescence radiation. All measurements were performed under vacuum conditions at 1.1 mbar with an accelerating voltage of 50 kV and a current of 600 $\mu$A. The X-ray energy spectra were collected in the range of 0−40 keV. The intensities of the following elements were obtained: K, Mg, Ce, Ca, and P. For each sample, 1,25,500 measurements were carried out for an area of 0.5 cm × 1.0 cm with a resolution of 20 $\mu$m and a measurement time of 250 ms per spot.

**2.7. Computational Details.** Calculations were performed using DFT within the generalized gradient approximation (GGA), as implemented in the Vienna ab initio Simulation Package (VASP).[22,23] The projector-augmented wave scheme (PAW)[24] was used to describe the electron-ion interaction,[25] whereas the electronic wave functions were expanded into plane waves with kinetic energy up to 400 eV for the structures with $KH_2PO_4$ and $MgNH_4PO_4·6H_2O$ and up to 540 eV for the structures with $CePO_4$. The PBE functional was used to describe the electron exchange and correlation interactions within the GGA.[26] The Si(111) surface was modeled by periodically repeated slabs of 6 atomic layers, with a vacuum region equivalent to 14 atomic layers. All the layers except the layers of silicon were allowed to relax until tolerances of $10^{-5}$ eV and 10 meV $Å^{-1}$ in the energies and forces, respectively. Brillouin zone integration was performed using a 4 × 4 × 1 k-mesh within the Monkhorst−Pack scheme.[27]

It is well known that standard approximations to DFT may incorrectly capture the electronic structure of materials with localized d and f states. In this work, for models concerning CePO4, we used a DFT + $U$ framework, described by Dudarev et al.[28] to correct the self-interaction errors associated with the Ce 4f states.[29−32] The nominal charge on cerium in $CePO_4$ is $Ce^{3+}$, leaving one 4f electron on each cerium atom. The highly localized nature of these 4f states demands special consideration for the electronic structure of $CePO_4$. The ground-state geometry can be obtained with good accuracy using DFT-based methods and the impact of the strongly localized Ce 4f states with the effective Hubbard-like parameter $U_{eff}$. In this approach, the strong Coulomb repulsion between localized 4f states in Ce is treated by adding an effective Hubbard term to the Kohn−Shan Hamiltonian, leading to an improved description of correlation effects.[33,34] DFT + $U$ requires two parameters, the Coulomb parameter $U$ and the exchange interaction $J$. Because there is no unique way of including a Hubbard term within the DFT framework, different approaches may be adopted. Based on the analysis of the literature, the $U_{\mathrm{eff}} = U - J$ values for Ce 4f states in $CePO_4$ that provide the best match for experiments were between 2.5 and 3 eV. In our calculations, the $U_{\mathrm{eff}}$ value of 3 eV[35] was used.

To find the exact saddle point and the minimum energy path (MEP) between various initial phosphate interfaces and doped structures, transition state searches were carried out using the climbing image-nudged elastic band (CI-NEB) method implemented in VASP. To perform the NEB calculations for each diffusion path, 3 images of the system starting from the initial to the final state were used to find the minimum energy path. The energy barrier is then calculated by taking the difference between the highest energy of the transition state and the initial structure.[36]

## 3. RESULTS AND DISCUSSION

**3.1. Investigation of Tethering by Aggregation and Growth.** In addition to HAp, three different minerals were chosen to investigate the homogeneity dependence on the type of mineral used, number of mineral particles, size of particles, and rate of evaporation of the liquid used to prepare the dispersion of mineral particles. Thus, the T-BAG process was further investigated with the previously used hydroxyapatite as a dopant, as well as with three new minerals. Figure 1 illustrates the different stages of the MID process, showing a schematic representation of the interfaces and their transformations during the T-BAG process, the annealing step, which leads to a formation of metal silicates while phosphorus diffuses into silicon bulk, and the possibility of the etching process without the use of highly toxic chemicals.

The thickness of the deposited film has a direct impact on the performance and properties of the rapid thermal annealing process and diffusion of phosphorus into the silicon bulk as well as on the etching step. Therefore, it must be carefully considered and controlled during the preparation of the mineral layers on top of a silicon layer. To investigate the influence of the thickness of the deposited films, two directions of the T-BAG process were investigated: the T-BAG process in which a mineral solution or a mineral dispersion is used.

For the T-BAG process in which a mineral dispersion is used, the most important factor in achieving a uniform distribution of particles on the surface is the size of the particles of the minerals used. To yield a fine size of particles, the minerals were crushed and ground by a pestle and mortar with the subsequent preparation of dispersion in THF. To achieve an even finer size of mineral particles, a sonotrode was used. A clean wafer was immersed in the dispersion of the mineral and THF. The dispersion was heated at 60 °C until complete evaporation (≈2 h) of the liquid, and the mineral particles covered both sides of the wafer surface. It was found that the rate of evaporation did not influence the homogeneity of the sample. However, the volume of the liquid above the silicon wafer has a direct impact. It is believed that during the evaporation of THF, the system cools down, and a certain time is required to achieve the same temperature throughout the entire volume of the dispersion.

To investigate the T-BAG process using a mineral solution and see the feasibility of achieving the nanoscale size of mineral particles, the dispersions of HAp in THF were left undisturbed for 12 h to allow bigger particles under the influence of gravitational force to move toward the bottom of the test tube. Afterward, the sediment and clear liquid above the sediment were observed. The clear liquid above the sediment would be referred to as a solution of HAp as no particles were visible. Aliquots of different volumes were taken to prepare samples of solutions of HAp at different concentrations. Immersing piranha-cleaned Si wafers into such solutions of 3 different concentrations allowed the T-BAG process to be carried out, leading to the deposition of mineral films on the silicon surface. Such an experiment allowed to obtain layers of minerals consisting of nanoscale sizes of mineral particles. To confirm the presence of nanoparticles on the surface of silicon wafers, SE and FT-IR spectroscopy were performed.

We performed SE measurements on thin films of hydroxyapatite of several thicknesses and correlated the thicknesses of each sample with their corresponding intensity of FT-IR measurements. FT-IR measurements were referred to as the cleaned wafer. The linear dependence of the intensity of the IR signal and the thickness of deposited mineral layers can be observed. The amount of deposited phosphate can be found through the intensity of the phosphate signal (at 1105 $cm^{-1}$, spectra are not shown in the article) and SE measurements of the thickness of the mineral film (the spectra are not shown here). For hydroxyapatite, three mineral films with various thicknesses (3.0, 3.5, and 4.4 nm) were obtained. To confirm a uniform distribution of the mineral particles of hydroxyapatite on both sides of the wafer $\mu$XRF mapping was performed, allowing the spatially resolved evaluation of film uniformity (see Supporting Information, S-4). The intensity of the IR suggests that the physisorbed mineral surface is covered by multilayers. Given the assumption that the coverage of the silicon wafer by mineral particles is uniform and that the layers of HAp on Si wafers have the same density as HAp crystals, the amount of hydroxyapatite deposited on top of the silicon wafer can be calculated through the value of the density of 3.08 g/$cm^3$. Knowing the area of the wafer (2 sides) and multiplying it by the thickness of the layers (obtained through SE), we can calculate the total volume of the layer. Then the volume of the HAp layer on both sides of the wafer is multiplied by the density of HAp. Based on the above-mentioned assumptions, it was calculated that three thin films of hydroxyapatite were obtained with the following amount of HAp:[37] 5.6 $\mu$g, 6.4 $\mu$g, and 8.2 $\mu$g. Knowing the mass of HAp on the sides of wafers, it is possible to find the number of moles of HAp deposited, then using Avogadro's number, one can convert mass of HAp deposited on the sides of Si wafer into the concentration of phosphate particles per $cm^2$, which yields the following values: $3.3 \times 10^{15}$, $3.8 \times 10^{15}$, and $4.9 \times 10^{15}$, respectively. In addition, thin films of $KH_2PO_4$, $MgNH_4PO_4{\cdot}6H_2O$, and $CePO_4$ were prepared. Through the calibration measurements of thin films of HAp through SE and the intensity of the IR signal, by measuring the intensity of the IR signal for the phosphate group, we were able to determine the amount of phosphorus containing in the thin films of mineral particles deposited on the silicon surface. $KH_2PO_4$, $MgNH_4PO_4{\cdot}6H_2O$, and $CePO_4$ yield $3.5 \times 10^{16}$, $5.1 \times 10^{17}$, and $5.9 \times 10^{17}$ $PO_4^{3-}$ particles/$cm^2$ respectively.

To understand the mechanism of the deposition of thin films of phosphate mineral particles, several factors need to be considered. A surface immersed in a solution or a liquid usually acquires a charge,[38] which attracts counterions and repels co-ions to form an electrical double layer. The ions directly adsorbed to the surface are referred to as the Stern layer.[39] The surface charge may be acquired via the protonation/deprotonation of surface groups, ion adsorption to or desorption from the surface, ion exchange between the surface

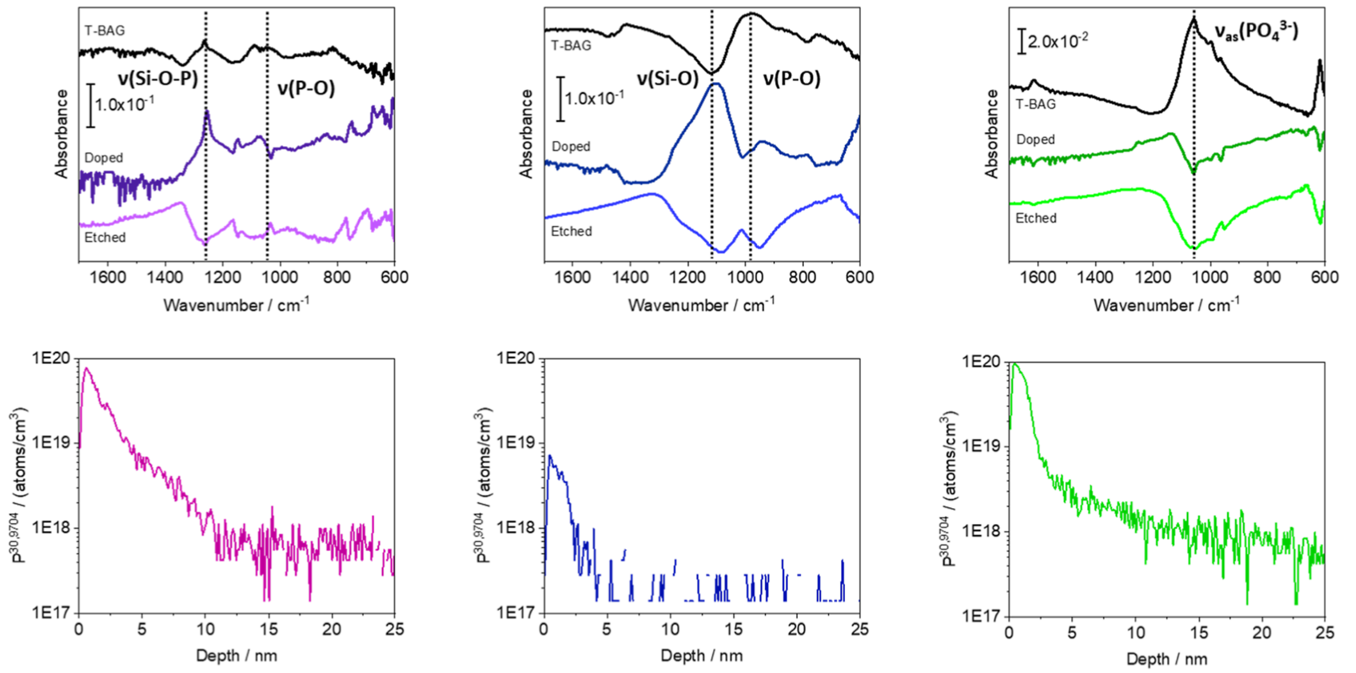

**Figure 2.** Upper panel: FT-IR spectra of $KH_2PO_4$, $MgNH_4PO_4{\cdot}6H_2O$, and $CePO_4$ on Si(111) after (1) the T-BAG process (black color), the measurements are referenced to as the cleaned wafer, (2) annealing at 900 °C (purple-dark for K; blue-dark for Mg; green-dark for Ce), the measurements are referred to as the wafer after carrying out the T-BAG process, and (3) etching (purple for K; blue for Mg; and green for Ce), the measurements are referred to as the wafer after carrying out the annealing process. Lower panel: ToF-SIMS of the $KH_2PO_4$/Si, $MgNH_4PO_4{\cdot}6H_2O$/Si, and $CePO_4$/Si interfaces (from left to right) after the samples were heated to 900 °C and etching them subsequently. ToF-SIMS profiles of P in doped Si(111) were obtained using the P concentration. Clear incorporation of phosphorus into the Si after heating the mineral-terminated samples can be observed, with most of the P being detected by SIMS.

and the solution.[40] As the silicon wafers were cleaned with a piranha solution and then rinsed with DI water, the surface of silicon wafers terminated with the native chemical oxide is negatively charged. In carrying out the T-BAG process, THF was used, which is a moderately polar solvent; then, the specific adsorption of ions needs to be considered. Once the dispersion of $KH_2PO_4$ in THF is left undisturbed for at least 12 h, a clear liquid was obtained. Given that potassium phosphate monobasic is soluble in THF, one can positively say that a solution of $KH_2PO_4$ was obtained; therefore, $KH_2PO_4$ particles exist in the solution in a dissociated state. With a high probability, it can be said as well that the formation of the Stern layer was taking place in the multilayers of minerals. However, HAp, $MgNH_4PO_4{\cdot}6H_2O$, and $CePO_4$ are poorly soluble, therefore, it could be assumed that the formation of multilayers of minerals was dominated by the size of the particles in the suspension via the Brownian motion.

To summarize both approaches, for an increased concentration of phosphate mineral particles, most of the particles did not dissolve and were suspended in the liquid, as expected. It is worth mentioning that the higher the concentration of the particles in the dispersion, the lower the homogeneity of the mineral thin films is. Such an observation was noted during the preparation of samples utilizing the T-BAG process. Such an observation is empirical and warrants further investigations in the future. The extensive analysis of the T-BAG method was done only for the HAp sample because HAp displays the highest uniformity of the particle size, as compared to $KH_2PO_4$, $MgNH_4PO_4{\cdot}6H_2O$, and $CePO_4$ samples. Such observations were concluded through $\mu$XRF mapping.

It is important to acknowledge that, as shown in Figure S-4 (see the Supporting Information), the lateral distribution of phosphorus across the surface varies significantly between precursors. $KH_2PO_4$, being highly soluble and molecularly dispersed, forms a homogeneous film during the T-BAG coating step, resulting in uniform phosphorus incorporation. In contrast, $CePO_4$ exhibits low solubility and forms larger particles, leading to an inhomogeneous deposition with a spotty coverage and localized doping.

Thus, both the solubility and particle size of the mineral precursors critically affect the quality and reproducibility of the doping process through their impact on the initial film formation.

The current section deals with the investigation of the T-BAG method and feasibility of obtaining layers of mineral particles with varied thicknesses. During this investigation, four minerals were used. However, the next sections exclude the nanoscale size of mineral particles deposited on Si wafers. Additionally, the next sections concern only $KH_2PO_4$, $MgNH_4PO_4{\cdot}6H_2O$, and $CePO_4$ as hydroxyapatite was investigated in the previous work.[7]

### 3.2. Etching, Processing, and Doping Limits.

To investigate the phases formed on the surface of silicon wafers and the feasibility of performing etching processes without the use of HF, the following experiments were carried out. Si wafers were cleaned according to the procedure described in the Methods Section. Each clean Si wafer was labeled to reference the same wafer after each FT-IR measurements and for each mineral thin film prepared via the T-BAG process. Subsequently, the samples were subjected to rapid thermal annealing at 900 °C for 1 min. The samples were immersed into a piranha solution for 30 min at 80 °C and rinsed afterward. After each step, FT-IR spectra were taken.

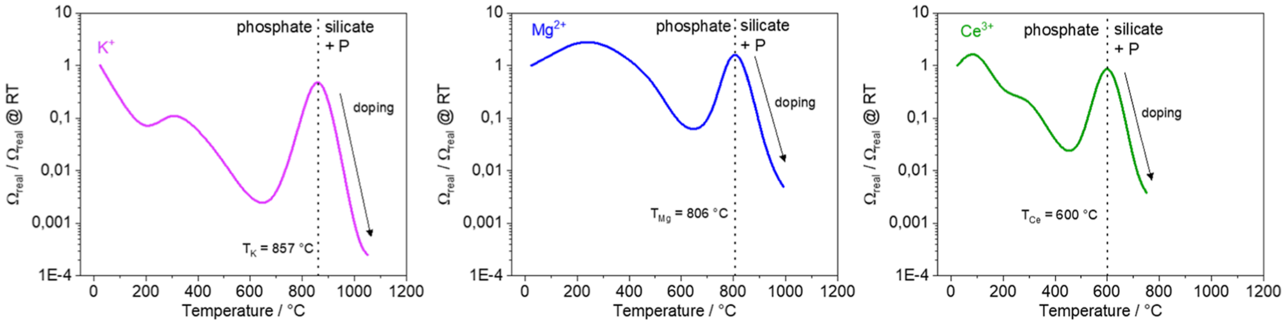

**Figure 3.** Resistance of the sample measured by EIS. Samples were stepwise increased in temperatures up to 800 °C, keeping the temperature at each step for 30 s and then allowing the system to cool down again to the initial temperature. The three lines present changes in the electrical resistance based on (chemical) processes happening at different temperatures. Please note that in the green line ($Ce^{3+}$) all points have been measured. In the blue line ($Mg^{2+}$) and magenta line ($K^+$), one point at the highest temperature is added from a mathematical fitting; following the full width at the half-maximum of the peak and the slope of the lines from low temperatures.

In Figure 2, the differential spectra are depicted, showing the corresponding IR spectra as a function of the processing step. First, the reference IR measurements of cleaned silicon samples were taken, and, subsequently, the T-BAG process was carried out, and a second IR measurement was taken. Figure 2 (upper panel) shows the adsorption of $KH_2PO_4$, $MgNH_4PO_4{\cdot}6H_2O$, and $CePO_4$ on Si(111). After the annealing process was carried out at 900 °C for all three minerals, the IR measurements of the samples were recorded again with the previous IR measurements of the wafers after carrying out the T-BAG process being used as a reference. The selected bands correspond to Si−O−P asymmetric stretching (~970−1010 $cm^{-1}$), Si−O stretching modes (~1040−1100 $cm^{-1}$), P−O stretching vibrations (~950−990 $cm^{-1}$), and $PO_4^{3-}$ group modes (~550−600 $cm^{-1}$ and ~1020−1100 $cm^{-1}$).[41,42] The chemical transformation of phosphate in contact with silicon can be observed, and the formation of the metal silicate can also be detected. During the final etching step (using the IR measurements of the samples after performing the annealing process as a reference), the disappearance of silicates (1000−1200 $cm^{-1}$), whereas peaks associated with chemical silicon oxides (800−1000 $cm^{-1}$) appear on the spectra.

Besides IR, ToF-SIMS is an important measurement method to quantitatively assess the doping process. In addition, the penetration depth can also be measured. Figure 2 (bottom panel) shows the obtained results for phosphorus dopant atoms in silicon wafers. Notably, at the depth between 0 and 5 nm, there is a significant amount of oxygen contamination as the samples were processed by RTA, piranha solution, in an oxygen-containing environment. As a future improvement, the samples can be annealed in a reducing atmosphere. Mg-containing mineral exhibits a much lower concentration, as compared to K- and Ce-containing minerals. The most likely reason is the smaller amount of Mg-containing mineral deposited on the silicon wafer compared with the other two investigated minerals. MID[7] was previously investigated for $Ca^{2+}$ ions, and it was shown that there is a clear influence of the metal ion on doping behavior. One of the reasons could be due to the difference in the mechanism of formation of silicates during the transformation of the Si/mineral interface. Investigations of the duration and temperature of annealing should be performed in order to determine the optimal regime of doping. Nevertheless, under the conditions described in the Methods Section, the doping of Si wafers with phosphorus can be positively confirmed. It is important to note that during ToF-SIMS measurements bulk microdefects on the surface of the etched silicon wafers were observed. Analysis of such spots showed a high concentration of phosphorus, which is common during the diffusion of phosphorus in silicon.[43,44] However, during ToF-SIMS measurements, areas with bulk defects were avoided.

EIS measurements give important inputs about the doping process. Silicon wafers were first mechanically and chemically cleaned, and the T-BAG process for the phosphates ($KH_2PO_4$, $MgNH_4PO_4{\cdot}6H_2O$, and $CePO_4$) was carried out. The next step consisted of a stepwise increase of the temperature up to 800 °C, keeping the temperature at each step for 30 s and then allowing the system to cool again to the initial temperature. After each step, EIS measurements at room temperature were taken. From the impedance plots (not shown here), indicating a specific electrical behavior, after heating the samples to 600−750 °C, a notable transformation occurred, and the size of the semicircles was reduced by a factor of a thousand. These observations suggest intricate changes in the electrical properties of the material, possibly linked to the phosphorus doping process or structural modifications induced at elevated temperatures. Based on the Nyquist plots, the drop in resistance for each of the minerals ($KH_2PO_4$, $MgNH_4PO_4{\cdot}6H_2O$, and $CePO_4$ on Si(111)) was found as a function of the temperature. Figure 3 shows the resistance of the samples measured by EIS. The three plots show changes in electrical resistance as a function of the temperature. The most interesting behavior is observed for $CePO_4$. Indeed, the resistance of the first sample drops with increasing temperatures but increases at 600 °C. As the EIS measurements give the output for the overall sample, i.e., the Si(111) wafer, as well as cerium silicate phases on the surface of the wafer, there might be two competing processes such as a conductivity of the doped sample as well as high resistance of the cerium silicate and/or silicon oxide phases on the surface. However, further investigations are warranted in order to understand which process predominates. In Figure 3, a predictive model of temperature dependence of the doping process based on various metal phosphates is presented. As $CePO_4$ displays the lowest temperature at which doping of silicon with phosphorus can be observed, a mathematical fitting was performed for the other two minerals. The mathematical fitting was based on the full width at half-maximum of the peak and the slope of the lines from low temperatures. Based on the fitting, the doping temperatures of silicon with phosphorus for potassium and magnesium phosphate minerals can be obtained. As shown in

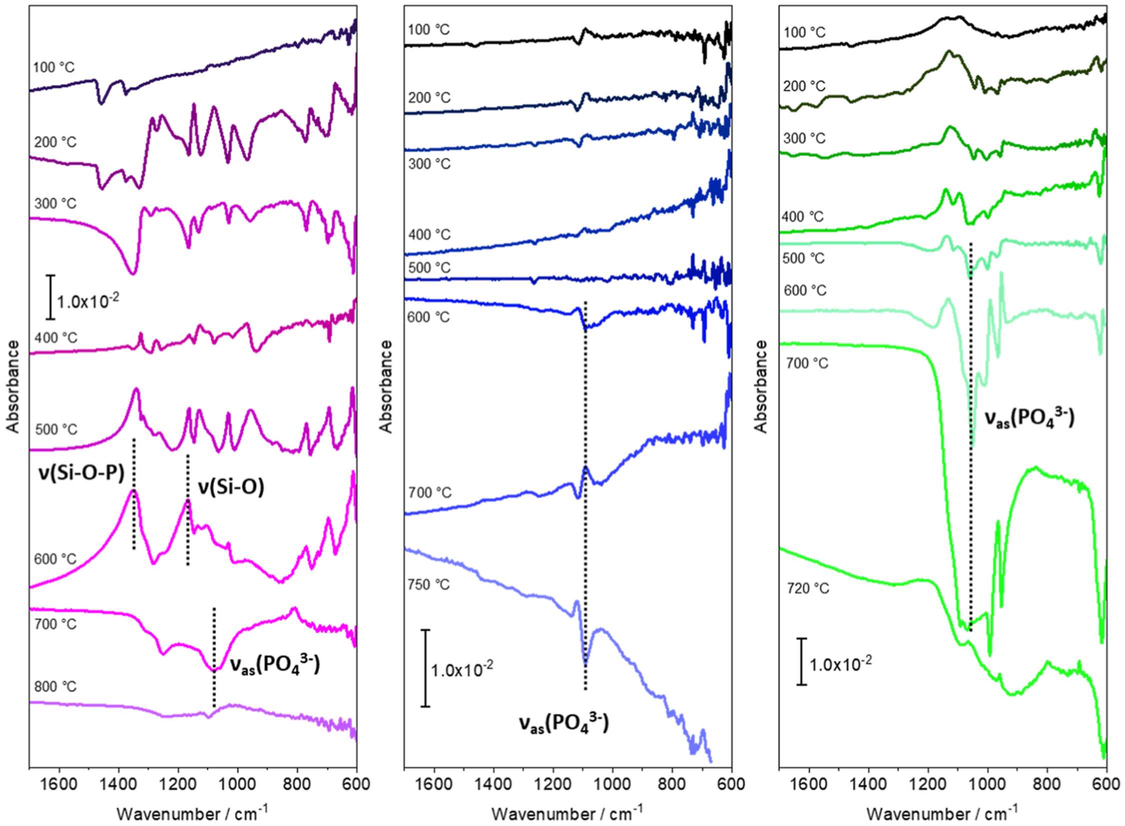

**Figure 4.** FT-IR spectra of $KH_2PO_4$ (left), $MgNH_4PO_4{\cdot}6H_2O$ (middle), and $CePO_4$ (right) as a function of the temperature. Measurements were always taken at room temperature. The samples of minerals deposited on silicon wafers were stepwise heated to the temperatures displayed in the image, with the spectra always referring to the previous temperature.

Figure 3, the doping process begins at 857 °C for $K^+$ and 806 °C for $Mg^{2+}$.

Another point that is worth addressing here is whether all of the deposited phosphate mineral would be consumed during the reaction with the silicon oxides on the surface of the silicon wafer. Further experiments would be required to investigate whether, at least for nanofilms of phosphate particles, annealing leads to the consumption of the native oxide, resulting in the direct formation of metal silicates on the surface of silicon wafers.

Overall, the etching process with the piranha solution is not ideal, as it has strong oxidizing properties, leading to the oxygen contamination of the samples. However, performing a doping process at a higher temperature should lead to a deeper profile of phosphorus due to the higher number of particles that can overcome the diffusion kinetic barrier, while most of the metal ions and oxygen have a very limited solubility in silicon at high temperatures, which thermodynamically favors their remaining at the surface layer rather than diffusion into the silicon substrate.

### 3.3. Experimental Doping of Si Wafers.

To investigate the effects of different valence metal cations on the temperature dependence of doping silicon with phosphorus, we chose phosphates of metal cations with +1, +2, and +3 charge states. Silicon wafers were first mechanically and chemically cleaned and the T-BAG process for the phosphates ($KH_2PO_4$, $MgNH_4PO_4{\cdot}6H_2O$, and $CePO_4$) was subsequently carried out. The next treatment of the samples consisted of a stepwise increase of the temperature up to 800 °C, keeping the temperature at each step for 30 s and then allowing the system to cool down again to the initial temperature. Such a treatment of the samples was conducted inside the vacuum chamber. Figure 4 shows the corresponding FT-IR spectra as a function of the temperature for each phosphate. The spectra always refer to the previous temperatures in order to differentiate the changes corresponding to each separate heat step.

The nature of surface transformations and thermal decomposition reactions of $KH_2PO_4$ is more complex than those of the other two considered minerals. Monopotassium dihydrogen phosphate can exist in several polymorphs. A variety of condensed phosphates are formed, with the loss of water, at temperatures dependent upon the physical state of the sample, the nature of the surrounding atmosphere, and the temperature program applied.[45] As mentioned above, at room temperature, $KH_2PO_4$ has a tetragonal crystal structure.

At temperatures higher than 100 °C, the transformation of the chemical native silicon oxide into the thermal oxide and further changes in vibrational modes can be observed for the three minerals studied. Vibrational modes evidence these changes on the native oxide. As the temperature increases and a longer time is applied, the vibrational modes remain active but less intensive with every additional heating step.[46]

Heating crystals up to 190 °C changes its structure to monoclinic,[47] which can be observed in Figure 4 (left panel), through the appearance of multiple peaks. When heated further, $KH_2PO_4$ decomposes, by loss of water, to potassium (poly)metaphosphate, $KPO_3$, at temperatures between 300 °C and400 °C,[48] following the reaction

$$KH_2PO_4 \rightarrow KPO_3 + H_2O$$

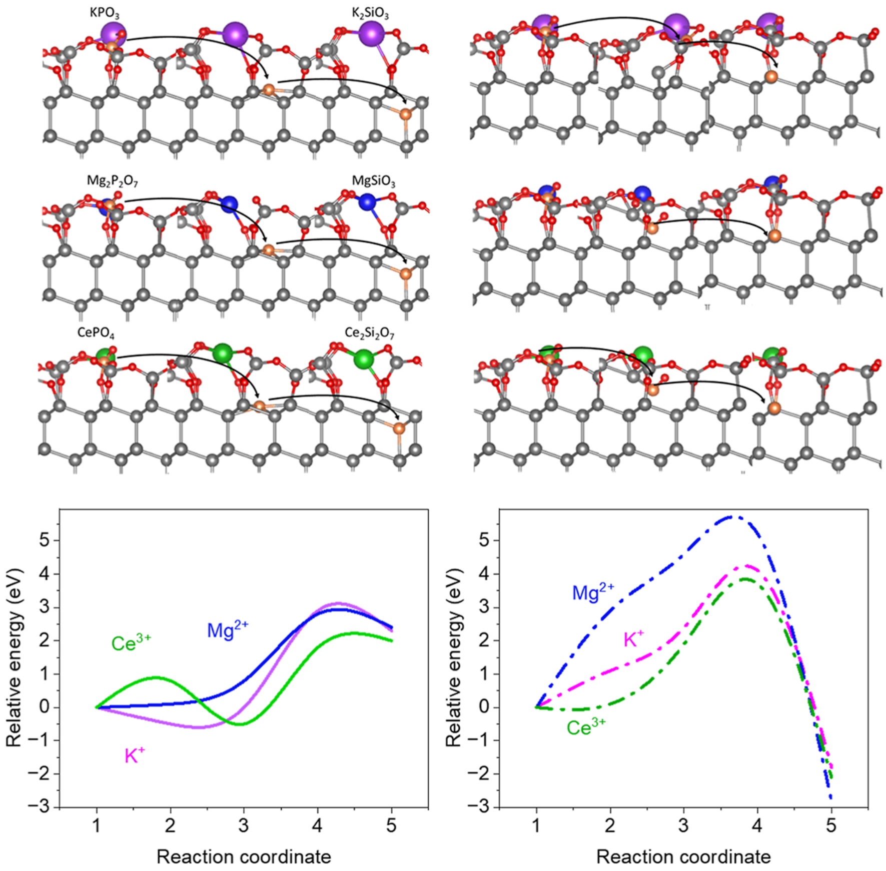

**Figure 5.** Upper panel: side-by-side display of NEB snapshots (initial, transition, and final state) for each system. All structures are shown in identical orientations to highlight the movement of the phosphorus atom across the interface. Side views of the phosphorus transport into a silicon (111) lattice lead to a hollow configuration (left) and an exchange configuration (right). Lower panel: kinetic evolution from the Si(111) interface containing a phosphate ion to the formation of the metal silicate at the interface and the doped structure. The peaks show the kinetic barriers of the reaction of diffusion of phosphorus. Gray spheres represent Si atoms; red, O; purple, K; blue, Mg; and green, Ce.

At temperatures above 400 °C, a reaction between potassium (poly)metaphosphate and the silicon oxide interface leads to the formation of phosphosilicate phases, which can be observed from the IR peaks at around 1320 $cm^{-1}$ ($\nu$(P–O–Si)) and 1150 $cm^{-1}$ ($\nu$(Si–O))

$$KPO_3 + SiO_x \rightarrow KSiP_3O_{10}$$

It can also be observed that changes in the transport of phosphorus into the silicon bulk do not happen until 700 °C

$$KSiP_3O_{10} + SiO_x \rightarrow K_2SiO_3 + P(\text{doped})$$

In the case of $MgNH_4PO_4{\cdot}6H_2O$, the FT-IR spectra are displayed in Figure 4 (middle panel). It is worth mentioning that for temperatures as low as 60 °C, the decomposition of struvite ($MgNH_4PO_4{\cdot}6H_2O$) can be observed with the loss of ammonia.[45,49] Given that the samples were prepared via the T-BAG procedure at 60 °C, it is accurate to say that the final composition of the mineral layer on the silicon wafer consists of $MgHPO_4$.[50] The overall decomposition reactions of $MgNH_4PO_4{\cdot}6H_2O$ are as follows

$$2MgNH_4PO_4{\cdot}6H_2O \rightarrow MgHPO_4 + 2NH_3 + 6H_2O \; (\text{below } 60\,°C)$$

$$Mg_2P_2O_7 + SiO_2 \rightarrow Mg_2SiP_4O_{12} \; (600\,°C)$$

$$Mg_2SiP_4O_{12} + SiO_x \rightarrow 2MgSiO_3 + P(\text{doped}) \; (700\,°C)$$

The presence of $NH_4^+$ in $MgNH_4PO_4$ leads to volatile decomposition products, preventing the formation of a stable solid phase on the wafer. This is reflected by the low number of P atoms/$cm^3$ measured with ToF-SIMS (Figure 2) and the low IR intensity of the phosphate (Figure 4).

For $CePO_4$ particles deposited on the silicon wafer, several observations can be made. After the sample is heated at 100 °C, loss of water can be observed, and a peak between 1280 and 950 $cm^{-1}$ occurs due to environment changes of $PO_4^{3-}$. Also, a shift of the P–O stretching vibrations at 1200 and 1000 $cm^{-1}$ to lower wavenumbers is observed. The IR spectra also show the decomposition of phosphate (1200–1050 $cm^{-1}$), as well as the formation of cerium silicate (1050–950 $cm^{-1}$). From the analysis of the $CePO_4$ differential FT-IR spectra, the following decomposition reaction can be proposed

$$CePO_4 + SiO_2 \rightarrow Ce_2Si_2O_7 + P(\text{doped}) \; (600\,°C)$$

The driving force for P diffusion into Si through the $SiO_2$ layer is the formation of P–$Si_3$ tetrahedra, which shows higher formation energy[51] compared to the surface P–$O_4$ species. However, the energy required to break the P–O4 bonds is relatively large; thus, a high-temperature regime—600 °C—is necessary in order to start the P diffusion into the bulk Si. Once started, the transport of phosphorus atoms across the $SiO_2$ layer is relatively fast, with a kinetic barrier of only 1.5 eV for P diffusion into the Si bulk.[51] Instead of undergoing evaporation, P atoms diffuse into the semiconductor host, driven by the concentration gradient, therefore doping the silicon wafer.

After heating the $CePO_4$ sample beyond 700 °C, new IR peaks appear between 630 and 1200 $cm^{-1}$, as a result of a surface transformation that indicates the formation of silicates on the surface of the silicon wafer. Additionally, the electronic activation changes notably, transforming the baseline of the silicon wafer.[52,53]

From the obtained IR spectra, it can be concluded that $CePO_4$ shows the most interesting properties, in order to be used as a dopant to enhance the electronic properties, of silicon. For instance, it shows the lowest doping temperature (600 °C) within the framework of MID. Overall, the process of formation of metal silicates in contact with silicon oxide is mainly thermodynamically driven, as was investigated for calcium silicate phases, such as wollastonite ($CaSiO_3$).[54,55] The great advantage of these phases as reaction products is that they do not require HF to be etched in the last step of semiconductor processing; mineral acids such as HCl or $H_2SO_4$ suffice for the etching process.[56]

### 3.4. Simulations of Diffusion of Phosphorus into the Silicon Lattice.

We intend to shed light on P diffusion into crystalline Si by investigating the atomistic mechanisms. The CI-NEB method[36] is used in this work to understand changes in the minimum energy path and activation barriers. The initial and final states are both local minimums in the potential energy surface. These states were obtained by inserting the P atoms in various positions within the silicon bulk, and then energy minimization calculations were performed. Figure 5 shows the type of P atom movements studied in this work. A single P atom as a part of the phosphate ion is allowed to be reduced and diffused into the silicon bulk. One of the studied pathways involved the interaction of the phosphate species with the native oxide surface, subsequent reduction, and diffusion of phosphorus in between the silicon atoms. This pathway is termed a hollow configuration. The P atom displacement is shown within the structures in Figure 5 (left panels). The other pathway studied involves the interaction of P with the silicon oxide interface and the exchange reaction with one of the silicon atoms from the silicon bulk, leading to an exchange in position between P and one of the Si atoms, which is referred to as an exchange configuration. This pathway is shown in the right panels of Figure 5. The Si atom participating in the exchange reaction is displaced from the silicon bulk onto the surface via the formation of a silicate. Figure 5 shows the energy diagrams for the P displacement following both pathways. It can be noted that the activation energy depends on the charge of metal cations as well as ion radii. The activation energy decreases with increasing metal charge and for smaller ionic radius. The energy diagrams also show that there is an intermediate state between the initial and final positions.

Even though the exchange configuration reaction pathways lead to an exothermic byproduct, the activation barrier is relatively high. Thus, at the experimentally observed doping temperatures, the hollow reaction pathway is more likely. As can be seen in Figure 5, $CePO_4$ displays the lowest activation barrier for both pathways, which agrees with the experimental data. The transition state shows that there is a partial reduction of the phosphate ion and incorporation of the phosphate radical into the silicon oxide layer. Therefore, the phosphate radical reduction at the $Si/SiO_2$ interface via $PO_x$ formation is the most likely pathway for phosphorus diffusion through the silicon oxide. Figure 5 also shows that P transport into Si(111) in the presence of $K^+$ ions is initially spontaneous. This is due to the energy differences in silicate formation as a function of the charge of metal ions, indicating that potassium metaphosphate is easily formed but leads to a metastable state.

The anomalously low onset temperature observed for $CePO_4$ may originate from the distinct electronic structure of $Ce^{3+}$. In contrast to closed-shell cations such as $Mg^{2+}$ or $K^+$, $Ce^{3+}$ possesses a partially filled $4f^1$ configuration. This can facilitate redox activity and electronic polarization at the interface, potentially promoting an earlier release or transfer of phosphate-derived species. Moreover, $Ce^{3+}$ is known to readily fluctuate between $Ce^{3+}$ and $Ce^{4+}$ under mildly oxidative conditions, which may activate interfacial reactions via electron-transfer mechanisms that do not occur for other cations.

In addition, $Ce^{3+}$—O bonds tend to be more labile compared with transition or alkaline earth metals, allowing for easier ligand exchange or condensation reactions with Si—OH surface groups. This may lead to the earlier formation of interfacial P—O—Si linkages.

While our current DFT analysis focuses on the energetic barriers for P diffusion in the oxide matrix, future work will focus on modeling the specific Ce—O—P—O—Si interface. Nevertheless, based on these observations, we hypothesize that other rare-earth elements (e.g., $La^{3+}$, $Nd^{3+}$, $Sm^{3+}$), which share comparable f-electron behavior and coordination chemistry, may show similar low-temperature doping profiles—a promising direction for environmentally benign doping strategies using naturally abundant phosphates.

To further elucidate the mechanistic role of the metal cations during the interface reaction, we performed Bader charge analysis on both the initial and the final geometries obtained from the NEB calculations. Table 1 summarizes the partial charges of the phosphorus atom and the respective metal ions ($K^+$, $Mg^{2+}$, and $Ce^{3+}$). The results indicate that during the transition phosphorus experiences a significant change in charge density, which is more pronounced in the

**Table 1. Bader Charge Analysis on Both the Initial and Final Geometries Obtained from the NEB Calculations**

| | | | Bader charge of P | Bader charge of the metal |
|---|---|---|---|---|
| K | exchange configuration | initial | 1.386901 | 6.102810 |
| | | doped | 5.102095 | 6.105583 |
| | hollow configuration | initial | 1.367761 | 6.099469 |
| | | doped | 5.774022 | 6.103804 |
| Mg | exchange configuration | initial | 1.360869 | 6.261227 |
| | | doped | 5.203158 | 6.265205 |
| | hollow configuration | initial | 1.370210 | 6.261024 |
| | | doped | 5.792085 | 6.239311 |
| Ce | exchange configuration | initial | 1.374703 | 10.394050 |
| | | doped | 5.199347 | 10.350113 |
| | hollow configuration | initial | 1.378292 | 10.390803 |
| | | doped | 5.797977 | 10.374431 |

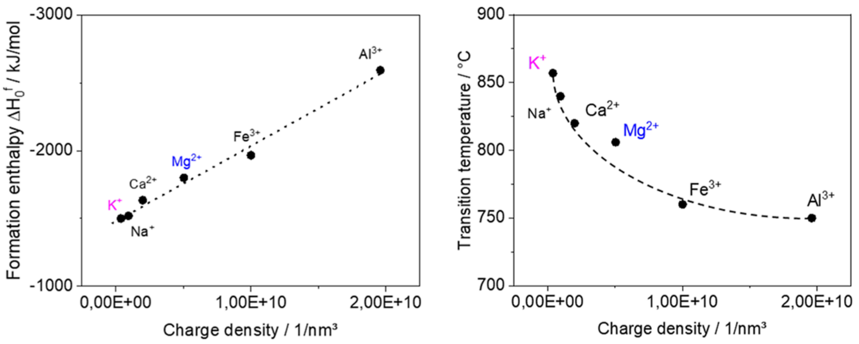

**Figure 6.** Left panel: standard formation enthalpy of silicates of metals vs charge density of metal ions (charge/cubed radius of metal ion) and right panel: temperature when a metal ion switches from a phosphate environment to silicate one and diffusion of phosphorus in Si bulk starts vs charge density of metal ions (charge/cubed radius of metal ion).

presence of high-valence cations such as $Ce^{3+}$. Simultaneously, the metal ions also exhibit a redistribution of charge, suggesting their active involvement in stabilizing intermediate states. These observations reinforce the interpretation that the ionic charge density ($z/r^3$) not only influences lattice thermodynamics but also modulates local electrostatics and charge delocalization at the interface—thereby tuning the reaction barrier.

**3.5. P-Doping Dependence on the Phosphate-Ion Charge Density.** To examine in-depth the role of metal ions in the doping process and understand the onset temperature of interfacial compound formation between metal phosphates and silicon oxide on the Si wafers, we systematically coated the substrates with different component phosphates (e.g., $KH_2PO_4$, $MgNH_4PO_4$, and $CePO_4$), as described in the Methods Section. Upon controlled heating, we monitored the electrical changes in the wafer using EIS. A sudden drop in resistance typically indicates the formation of a new interfacial phase (see Figure 3). Plotting the reaction temperatures against the ionic charge density ($z/r^3$) of the involved metal cations reveals a clear trend, as can be seen in Figure 6. The ionic radii used are shown in Table 2.[57−59] Then, the reaction threshold temperature ($T_{tr,Me}$) can be modeled using an exponential decay function with a saturation limit, reflecting both the thermodynamic barrier of the interface reaction and the influence of ionic properties (eq 1). As mentioned above, the driving force for P diffusion into Si through the $SiO_2$ layer is the formation of $P-Si_3$ tetrahedra, which shows higher formation energy than that of surface $PO_4$ species. The energy required to break the $P-O_4$ bond is relatively large; thus, a high-temperature regime—700 °C—is necessary to trigger the P diffusion process into the bulk Si.[7,60] Once started, the transport of phosphorus atoms across the $SiO_2$ layer is relatively fast, with a kinetic barrier of only 1.5 eV for P diffusion into the Si bulk.[51] However, according to the results obtained in this paper for different phosphates, the ionic charge density of the metal shows a clear influence on the temperature necessary for the interface reaction to reduce to phosphates. Such a temperature can be described with the following equation

$$T_{\mathrm{tr,Me}} = a \cdot e^{-b \cdot z / r^3} + c \qquad (1)$$

where $a$ is a factor determining extra energy required for diffusion in weakly binding systems (smaller value of $z/r^3$), $b$ is the steepness of temperature drop stemming from higher ionic bond strength, and $c$ is the absolute minimum temperature required to observe the diffusion of phosphorus into Si bulk.

**Table 2. Ion Radii, Charge Density of Selected Metal Ions, and Standard Formation Enthalpy of Silicates of Metals**

| ion | ionic radius (Å) | charge density $\left(\frac{z}{r^3} / \frac{1}{\mathrm{nm}^3}\right)$ | standard formation enthalpy of silicates of metals (kJ/mol) | temperature necessary for the interface reaction to reduce to phosphates, $T_{tr,Me}$ (°C) |
|---|---|---|---|---|
| $K^+$ | 1.38 | $3.80 \times 10^8$ | −1500.03 | 857 |
| $Na^+$ | 0.95 | $9.42 \times 10^8$ | −1518.79 | 840 |
| $Ca^{2+}$ | 0.99 | $2.00 \times 10^9$ | −1634.94 | 820 |
| $Mg^{2+}$ | 0.65 | $5.04 \times 10^9$ | −2174.01 | 806 |
| $Fe^{3+}$ | 0.63 | $1.00 \times 10^{10}$ | −1965.78 | 760 |
| $Al^{3+}$ | 0.67 | $1.96 \times 10^{10}$ | −2593.24 | 750 |

It is important to emphasize that this temperature reflects a surface reaction threshold, likely corresponding to the formation of elemental phosphorus or phosphate-derived species at the interface—and not the subsequent diffusion of these species into the silicon lattice. To validate this model equation, the standard formation enthalpies of metal silicates versus charge densities of metal ions in phosphate minerals are plotted in Figure 6 (left panel), together with the doping temperature (right panel) dependence on charge densities of metal ions. The obtained dependence suggests that the initial temperature for phosphorus diffusion into Si bulk is determined by the process of switching metal ions between phosphate and silicate environments.

Equation 1 captures the trend between the ionic charge density ($z/r^3$) and the onset temperature for interfacial reactions in a series of structurally and chemically simple metal phosphates. It is particularly valid for nonredox-active cations with stable oxidation states (e.g., $K^+$, $Mg^{2+}$, and $Al^{3+}$) and similar coordination environments in their phosphate structures. However, the model does not account for: redox chemistry at the interface (as seen with $Ce^{3+}$, possibly deviating from the model), entropy-driven effects, or changes in surface kinetics. Therefore, the predictive power of eq 1 is best suited for comparing structurally similar metal phosphates and may not generalize to rare-earth or transition-metal-based phosphates, where additional interfacial or electronic effects dominate.

The model described above holds true for classical metal phosphates forming silicates, such as those based on K, Mg, and Al, where the interfacial reaction temperature is higher than the phosphorus transport temperature—making the reaction the rate-limiting step. However, doping with $CePO_4$ has shown an interfacial reaction temperature lower than the transport temperature of phosphorus, indicating that the rate-limiting step is shifted. This opens up new possibilities for controlled dopant incorporation into bulk lattices via tailored surface chemistry.

## 4. CONCLUSIONS

In this work, we have investigated the conditions for the performance and the mechanism of the T-BAG process for phosphorus-containing minerals in order to yield a better homogeneity of the mineral multilayers deposited on the surface silicon wafers. The thickness of the mineral layers can be as low as a few nanometers, as it was investigated in the case of HAp. The main advantage of controlling the thickness of the mineral multilayer is the ability to control the concentration of the diffused phosphorus into the silicon bulk.

In addition, we have extended the investigation about the mineral interface doping by carrying out the annealing process for the phosphates of metal cations with +1, +2, and +3 charges to determine whether there is a temperature dependence of doping silicon. Our findings indicate that increasing the metal charge density of metal ions forming phosphate minerals leads to lower required doping temperatures. Interestingly, ions of rare-earth metals present in phosphate minerals can lead to significantly lower temperatures of diffusion of phosphorus in the Si bulk.

## ■ ASSOCIATED CONTENT

### Supporting Information

The Supporting Information is available free of charge at https://pubs.acs.org/doi/10.1021/acsami.5c09080.

> Information on differential infrared spectra, ToF-SIMS, EIS methods and interpretation, and quantitative micro-X-ray fluorescence ($\mu$-XRF) mapping for K, Mg, Ce, and Ca (PDF)

## ■ AUTHOR INFORMATION

### Corresponding Author

**Peter Thissen** − *Institute of Concrete Structures and Building Materials, Karlsruhe 76131, Germany;* orcid.org/0000-0001-7072-4109; Email: peter.thissen@kit.edu

### Authors

**Roman Konoplev-Esgenburg** − *Institute of Concrete Structures and Building Materials, Karlsruhe 76131, Germany;* orcid.org/0009-0003-2227-5590

**Meike Koenig** − *Institute of Functional Interfaces, Eggenstein, Leopoldshafen 76344, Germany;* orcid.org/0000-0003-3150-8723

**Alexander Welle** − *Institute of Functional Interfaces, Eggenstein, Leopoldshafen 76344, Germany; Karlsruhe Nano Micro Facility, Eggenstein, Leopoldshafen 76344, Germany;* orcid.org/0000-0002-3454-6509

**Andreas Bogner** − *Institute of Concrete Structures and Building Materials, Karlsruhe 76131, Germany*

**Roberto C. Longo** − *Tokyo Electron America, Inc, Austin, Texas 78741, United States;* orcid.org/0000-0003-4353-841X

Complete contact information is available at: https://pubs.acs.org/10.1021/acsami.5c09080

### Notes

The authors declare no competing financial interest.

## ■ ACKNOWLEDGMENTS

P.T. acknowledges the DFG for the financial support. The authors acknowledge support by the state of Baden-Württemberg through bwHPC.

## ■ REFERENCES

(1) Li, Y.; Yang, J.; Zhao, R.; Zhang, Y.; Wang, X.; He, X.; Fu, Y.; Zhang, L. Design of Organic-Inorganic Hybrid Heterostructured Semiconductors via High-Throughput Materials Screening for Optoelectronic Applications. *J. Am. Chem. Soc.* **2022**, *144* (36), 16656−16666.

(2) Hazut, O.; Agarwala, A.; Amit, I.; Subramani, T.; Zaidiner, S.; Rosenwaks, Y.; Yerushalmi, R. Contact Doping of Silicon Wafers and Nanostructures with Phosphine Oxide Monolayers. *ACS Nano* **2012**, *6* (11), 10311−10318.

(3) Hazut, O.; Huang, B.-C.; Pantzer, A.; Amit, I.; Rosenwaks, Y.; Kohn, A.; Chang, C.-S.; Chiu, Y.-P.; Yerushalmi, R. Parallel p-n Junctions across Nanowires by One-Step *Ex Situ* Doping. *ACS Nano* **2014**, *8* (8), 8357−8362.

(4) Ho, J. C.; Yerushalmi, R.; Jacobson, Z. A.; Fan, Z.; Alley, R. L.; Javey, A. Controlled Nanoscale Doping of Semiconductors via Molecular Monolayers. *Nat. Mater.* **2008**, *7* (1), 62−67.

(5) Ho, J. C.; Yerushalmi, R.; Smith, G.; Majhi, P.; Bennett, J.; Halim, J.; Faifer, V. N.; Javey, A. Wafer-Scale, Sub-5 Nm Junction Formation by Monolayer Doping and Conventional Spike Annealing. *Nano Lett.* **2009**, *9* (2), 725−730.

(6) Longo, R. C.; Cho, K.; Schmidt, W. G.; Chabal, Y. J.; Thissen, P. Monolayer Doping via Phosphonic Acid Grafting on Silicon: Microscopic Insight from Infrared Spectroscopy and Density Functional Theory Calculations. *Adv. Funct. Mater.* **2013**, *23* (27), 3471−3477.

(7) Thissen, P.; Longo, R. C. Mineral Interface Doping: Hydroxyapatite Deposited on Silicon to Trigger the Electronic Properties. *Adv. Mater. Interfaces* **2024**, *11* (31), 2400061.

(8) Itoh, Y.; Nozaki, T. Solubility and Diffusion Coefficient of Oxygen in Silicon. *Jpn. J. Appl. Phys.* **1985**, *24* (3R), 279.

(9) Johnston, M. D.; Khajavi, L. T.; Li, M.; Sokhanvaran, S.; Barati, M. High-Temperature Refining of Metallurgical-Grade Silicon: A Review. *JOM* **2012**, *64* (8), 935−945.

(10) *Celebrating the International Year of Mineralogy: Progress and Landmark Discoveries of the Last Decades*; Bindi, L., Cruciani, G., Eds.; Springer Mineralogy; Springer Nature Switzerland: Cham, 2023.

(11) Mills, S. J.; Hatert, F.; Nickel, E. H.; Ferraris, G. The Standardisation of Mineral Group Hierarchies: Application to Recent Nomenclature Proposals. *ejm* **2009**, *21* (5), 1073−1080.

(12) Hughes, J. M.; Rakovan, J. F. Structurally Robust, Chemically Diverse: Apatite and Apatite Supergroup Minerals. *Elements* **2015**, *11* (3), 165−170.

(13) Cook, R. B. Fleischer's Glossary of Mineral Species by Malcolm E. Back. The Mineralogical Record, PO Box 30730, Tucson, AZ 85751; www.mineralogicalrecord.com. 420 Pages; 2014; $34 (Spiral Bound). *Rocks Miner.* **2015**, *90* (4), 391.

(14) Pasero, M.; Kampf, A. R.; Ferraris, C.; Pekov, I. V.; Rakovan, J.; White, T. J. Nomenclature of the Apatite Supergroup Minerals. *ejm* **2010**, *22* (2), 163−179.

(15) Vega, A.; Thissen, P.; Chabal, Y. J. Environment-Controlled Tethering by Aggregation and Growth of Phosphonic Acid Monolayers on Silicon Oxide. *Langmuir* **2012**, *28* (21), 8046−8051.

(16) Schnetzer, F.; Thissen, P.; Giraudo, N.; Emmerich, K. Unraveling the Coupled Processes of (De)Hydration and Structural Changes in $Na^+$ -Saturated Montmorillonite. *J. Phys. Chem. C* **2016**, *120* (28), 15282−15287.

(17) Popere, B. C.; Russ, B.; Heitsch, A. T.; Trefonas, P.; Segalman, R. A. Large-Area, Nanometer-Scale Discrete Doping of Semi-

conductors via Block Copolymer Self-Assembly. *Adv. Mater. Interfaces* **2015**, *2* (18), 1500421.

(18) Hoarfrost, M. L.; Takei, K.; Ho, V.; Heitsch, A.; Trefonas, P.; Javey, A.; Segalman, R. A. Spin-On Organic Polymer Dopants for Silicon. *J. Phys. Chem. Lett.* **2013**, *4* (21), 3741−3746.

(19) Perego, M.; Seguini, G.; Arduca, E.; Nomellini, A.; Sparnacci, K.; Antonioli, D.; Gianotti, V.; Laus, M. Control of Doping Level in Semiconductors *via* Self-Limited Grafting of Phosphorus End-Terminated Polymers. *ACS Nano* **2018**, *12* (1), 178−186.

(20) Schnetzer, F.; Johnston, C. T.; Premachandra, G. S.; Giraudo, N.; Schuhmann, R.; Thissen, P.; Emmerich, K. Impact of Intrinsic Structural Properties on the Hydration of 2:1 Layer Silicates. *ACS Earth Space Chem.* **2017**, *1* (10), 608−620.

(21) Acik, M.; Lee, G.; Mattevi, C.; Chhowalla, M.; Cho, K.; Chabal, Y. J. Unusual Infrared-Absorption Mechanism in Thermally Reduced Graphene Oxide. *Nat. Mater.* **2010**, *9* (10), 840−845.

(22) Kresse, G.; Hafner, J. *Ab Initio* Molecular Dynamics for Liquid Metals. *Phys. Rev. B:Condens. Matter Mater. Phys.* **1993**, *47* (1), 558−561.

(23) Kresse, G.; Furthmüller, J. Efficient Iterative Schemes for *Ab Initio* Total-Energy Calculations Using a Plane-Wave Basis Set. *Phys. Rev. B:Condens. Matter Mater. Phys.* **1996**, *54* (16), 11169−11186.

(24) Blöchl, P. E. Projector Augmented-Wave Method. *Phys. Rev. B:Condens. Matter Mater. Phys.* **1994**, *50* (24), 17953−17979.

(25) Kresse, G.; Joubert, D. From Ultrasoft Pseudopotentials to the Projector Augmented-Wave Method. *Phys. Rev. B:Condens. Matter Mater. Phys.* **1999**, *59* (3), 1758−1775.

(26) Perdew, J. P.; Burke, K.; Ernzerhof, M. Generalized Gradient Approximation Made Simple. *Phys. Rev. Lett.* **1996**, *77* (18), 3865−3868.

(27) Monkhorst, H. J.; Pack, J. D. Special Points for Brillouin-Zone Integrations. *Phys. Rev. B:Condens. Matter Mater. Phys.* **1976**, *13* (12), 5188−5192.

(28) Dudarev, S. L.; Botton, G. A.; Savrasov, S. Y.; Humphreys, C. J.; Sutton, A. P. Electron-Energy-Loss Spectra and the Structural Stability of Nickel Oxide: An LSDA+U Study. *Phys. Rev. B:Condens. Matter Mater. Phys.* **1998**, *57* (3), 1505−1509.

(29) Da Silva, J. L. F.; Ganduglia-Pirovano, M. V.; Sauer, J.; Bayer, V.; Kresse, G. Hybrid Functionals Applied to Rare-Earth Oxides: The Example of Ceria. *Phys. Rev. B:Condens. Matter Mater. Phys.* **2007**, *75* (4), 045121.

(30) Fabris, S.; De Gironcoli, S.; Baroni, S.; Vicario, G.; Balducci, G. Taming Multiple Valency with Density Functionals: A Case Study of Defective Ceria. *Phys. Rev. B:Condens. Matter Mater. Phys.* **2005**, *71* (4), 041102.

(31) Kullgren, J.; Castleton, C. W. M.; Müller, C.; Ramo, D. M.; Hermansson, K. B3LYP Calculations of Cerium Oxides. *J. Chem. Phys.* **2010**, *132* (5), 054110.

(32) Martinez, U.; Giordano, L.; Pacchioni, G. Tuning the Work Function of Ultrathin Oxide Films on Metals by Adsorption of Alkali Atoms. *J. Chem. Phys.* **2008**, *128* (16), 164707.

(33) Da Silva, J. L. F.; Ganduglia-Pirovano, M. V.; Sauer, J. Formation of the Cerium Orthovanadate Ce V O 4: DFT + U Study. *Phys. Rev. B:Condens. Matter Mater. Phys.* **2007**, *76* (12), 125117.

(34) Nolan, M.; Parker, S. C.; Watson, G. W. The Electronic Structure of Oxygen Vacancy Defects at the Low Index Surfaces of Ceria. *Surf. Sci.* **2005**, *595* (1−3), 223−232.

(35) Adelstein, N.; Mun, B. S.; Ray, H. L.; Ross, P. N.; Neaton, J. B.; De Jonghe, L. C. Structure and Electronic Properties of Cerium Orthophosphate: Theory and Experiment. *Phys. Rev. B:Condens. Matter Mater. Phys.* **2011**, *83* (20), 205104.

(36) Henkelman, G.; Uberuaga, B. P.; Jónsson, H. A Climbing Image Nudged Elastic Band Method for Finding Saddle Points and Minimum Energy Paths. *J. Chem. Phys.* **2000**, *113* (22), 9901−9904.

(37) Saxena, A.; Pandey, M.; Dubey, A. K. Induced Electroactive Response of Hydroxyapatite: A Review. *J. Indian Inst. Sci.* **2019**, *99* (3), 339−359.

(38) Israelachvili, J. N. Electrostatic Forces between Surfaces in Liquids. In *Intermolecular and Surface Forces*; Elsevier, 2011; pp 291−340.

(39) Ricci, M.; Spijker, P.; Stellacci, F.; Molinari, J.-F.; Voïtchovsky, K. Direct Visualization of Single Ions in the Stern Layer of Calcite. *Langmuir* **2013**, *29* (7), 2207−2216.

(40) Gonella, G.; Backus, E. H. G.; Nagata, Y.; Bonthuis, D. J.; Loche, P.; Schlaich, A.; Netz, R. R.; Kühnle, A.; McCrum, I. T.; Koper, M. T. M.; Wolf, M.; Winter, B.; Meijer, G.; Campen, R. K.; Bonn, M. Water at Charged Interfaces. *Nat. Rev. Chem.* **2021**, *5* (7), 466−485.

(41) Nakamoto, K. *Infrared and Raman Spectra of Inorganic and Coordination Compounds: Part A: Theory and Applications in Inorganic Chemistry*, 1st ed.; Wiley, 2008.

(42) Mozzi, R. L.; Warren, B. E. The Structure of Vitreous Silica. *J. Appl. Crystallogr.* **1969**, *2* (4), 164−172.

(43) Fair, R. B.; Tsai, J. C. C. A Quantitative Model for the Diffusion of Phosphorus in Silicon and the Emitter Dip Effect. *J. Electrochem. Soc.* **1977**, *124* (7), 1107−1118.

(44) Cun, Z.; Jin, Q.; Li, S. Oxygen Precipitation Behavior and Its Influence on Phosphorus Gettering in Czochralski Silicon. *J. Cryst. Growth* **2024**, *648*, 127898.

(45) Saerens, B. *Thermal Decomposition of Struvite*; Springer, 2020.

(46) Tian, R.; Seitz, O.; Li, M.; Hu, W.; Chabal, Y. J.; Gao, J. Infrared Characterization of Interfacial Si-O Bond Formation on Silanized Flat SiO$_2$/Si Surfaces. *Langmuir* **2010**, *26* (7), 4563−4566.

(47) Itoh, K.; Matsubayashi, T.; Nakamura, E.; Motegi, H. X-Ray Study of High-Temperature Phase Transitions in KH$_2$ PO$_4$. *J. Phys. Soc. Jpn.* **1975**, *39* (3), 843−844.

(48) Brown, M. E.; Glasser, L.; Larson, J. High Temperature Thermal Properties of KH2PO4: Phase Transitions and Decompositions. *Thermochim. Acta* **1979**, *30* (1−2), 233−246.

(49) Ribbe, P. H. The Decomposition of Struvite: Further Evidence. *Mineral. Mag.* **1969**, *37* (286), 290−291.

(50) Paulik, F.; Paulik, J. TG and EGA Investigations of the Decomposition of Magnesium Ammonium Phosphate Hexahydrate by Means of the Derivatograph under Conventional and Quasiisothermal — Quasi-Isobaric Conditions. *J. Therm. Anal.* **1975**, *8* (3), 557−566.

(51) Thissen, P.; Cho, K.; Longo, R. C. Nanopatterning of Group V Elements for Tailoring the Electronic Properties of Semiconductors by Monolayer Doping. *ACS Appl. Mater. Interfaces* **2017**, *9* (2), 1922−1928.

(52) Longo, R. C.; Mattson, E. C.; Vega, A.; Cabrera, W.; Cho, K.; Chabal, Y. J.; Thissen, P. Mechanism of Arsenic Monolayer Doping of Oxide-Free Si(111). *Chem. Mater.* **2016**, *28* (7), 1975−1979.

(53) Kashkarov, V. M.; Goloshchapov, D. L.; Rumyantseva, A. N.; Seredin, P. V.; Domashevskaya, E. P.; Spivakova, I. A.; Shumilovich, B. R. X-Ray Diffraction and IR Spectroscopy Investigation of Synthesized and Biogenic Nanocrystalline Hydroxyapatite. *J. Synch. Investig.* **2011**, *5* (6), 1162−1167.

(54) Giraudo, N.; Krolla-Sidenstein, P.; Bergdolt, S.; Heinle, M.; Gliemann, H.; Messerschmidt, F.; Brüner, P.; Thissen, P. Early Stage Hydration of Wollastonite: Kinetic Aspects of the Metal-Proton Exchange Reaction. *J. Phys. Chem. C* **2015**, *119* (19), 10493−10499.

(55) Sanna, S.; Schmidt, W. G.; Thissen, P. Formation of Hydroxyl Groups at Calcium-Silicate-Hydrate (C-S-H): Coexistence of Ca-OH and Si-OH on Wollastonite(001). *J. Phys. Chem. C* **2014**, *118* (15), 8007−8013.

(56) Longo, R. C.; Cho, K.; Brüner, P.; Welle, A.; Gerdes, A.; Thissen, P. Carbonation of Wollastonite(001) Competing Hydration: Microscopic Insights from Ion Spectroscopy and Density Functional Theory. *ACS Appl. Mater. Interfaces* **2015**, *7* (8), 4706−4712.

(57) Maguire, M. E.; Cowan, J. A. Magnesium Chemistry and Biochemistry. *BioMetals* **2002**, *15* (3), 203−210.

(58) Shannon, R. D. Revised Effective Ionic Radii and Systematic Studies of Interatomic Distances in Halides and Chalcogenides. *Acta Crystallogr., Sect. A* **1976**, *32* (5), 751−767.

(59) Dean, J. A. *Lange's Handbook of Chemistry*, 12th ed.; MCGRAW-HILL: New York, 1979.

(60) Kc, S.; Dong, H.; Longo, R. C.; Wang, W.; Xiong, K.; Wallace, R. M.; Cho, K. Electronic Properties of InP (001)/HfO2 (001) Interface: Band Offsets and Oxygen Dependence. *J. Appl. Phys.* **2014**, *115* (2), 023703.

https://doi.org/10.1021/acsami.5c09080